Research Article | Vol. 28, No. 18 / 31 August 2020 / Optics Express 26953
Optics EXPRESS

Atmospheric correction in coastal region using same-day observations of different sun-sensor geometries with a revised POLYMER model

JUNWEI WANG,[1] ZHONGPING LEE,[2,*] JIANWEI WEI,[2,3] AND KEPING DU[4]

[1]State Key Laboratory of Marine Environmental Science, College of Ocean and Earth Sciences, Xiamen University, Xiamen 361102, China
[2]School for the Environment, University of Massachusetts Boston, Boston, MA 02125, USA
[3]NOAA Center for Satellite Applications and Research, Marine Ecosystems and Climate Branch, College Park, MD 20740, USA
[4]Beijing Key Laboratory for Remote Sens. Environ. and Digital Cities, Faculty of Geographical Science, Beijing Normal University, Beijing 100875, China
*zhongping.lee@umb.edu

Abstract: In this paper, with a revised POLYMER (POLYnomial based approach applied to MERIS data) atmospheric correction model, we present a novel scheme (two-angle atmospheric correction algorithm, termed as TAACA) to remove atmospheric contributions in satellite ocean color measurements for coastal environments, especially when there are absorbing aerosols. TAACA essentially uses the same water properties as a constraint to determine oceanic and atmospheric properties simultaneously using two same-day consecutive satellite images having different sun-sensor geometries. The performance of TAACA is first evaluated with a synthetic dataset, where the retrieved remote-sensing reflectance (R_{rs}) by TAACA matches very well (the coefficient of determination (R^2) ≥ 0.98) with the simulated R_{rs} for each wavelength, and the unbiased root mean square error (uRMSE) is ~12.2% for cases of both non-absorbing and strongly absorbing aerosols. When this dataset is handled by POLYMER, for non-absorbing aerosol cases, the R^2 and uRMSE values are ~0.99 and ~7.5%, respectively, but they are ~0.92 and ~39.5% for strongly absorbing aerosols. TAACA is further assessed using co-located VIIRS measurements for waters in Boston Harbor and Massachusetts Bay, and the retrieved R_{rs} from VIIRS agrees with *in situ* measurements within ~27.3% at the visible wavelengths. By contrast, a traditional algorithm resulted in uRMSE as 3890.4% and 58.9% at 410 and 443 nm, respectively, for these measurements. The R_{rs} products derived from POLYMER also show large deviations from *in situ* measurements. It is envisioned that more reliable R_{rs} products in coastal waters could be obtained from satellite ocean color measurements with a scheme like TAACA, especially when there are strongly absorbing aerosols.

1. Introduction

Since the Coastal Zone Color Scanner (CZCS) [1,2], a series of ocean color satellites have been successfully launched aiming for quantifying marine phytoplankton concentrations. Among others, the extensively used satellite ocean color data normally come from the Sea-viewing Wide Field-of-view Sensor (SeaWiFS) [3,4], the MODerate-resolution Imaging Spectroradiometer (MODIS) [5], the Medium Resolution Imaging Spectrometer Instrument (MERIS) [6] and the Visible Infrared Imager Radiometer Suite (VIIRS) [7]. At the top of atmosphere (TOA), these ocean color sensors after radiometric correction directly measure the radiance (L_t), which can be converted to TOA reflectance:

$$\rho_t(\lambda) = \pi L_t(\lambda)/\mu_0(\lambda)F_0(\lambda) \quad (1)$$

#393968 https://doi.org/10.1364/OE.393968
Journal © 2020 Received 31 Mar 2020; revised 1 Aug 2020; accepted 2 Aug 2020; published 28 Aug 2020

Optics EXPRESS

Here μ_0 and F_0 are the cosine of solar zenith angle and the extraterrestrial solar irradiance, respectively (definition of symbols used in this paper is included in Table 1). For the derivation of primary water constituents, firstly, the contributions from atmosphere and ocean surface must be removed through an atmospheric correction (AC) algorithm, yielding the water-leaving radiance (L_w). Because the magnitude of this radiance also varies with downwelling irradiance (E_d), water-leaving reflectance ($\rho_w = \pi L_w/E_d$), or remote-sensing reflectance ($R_{rs} = L_w/E_d$, sr^{-1}), is more commonly used. ρ_w and R_{rs} are interchangeable based on these definitions. Further, primary water properties in the upper layer, such as the chlorophyll concentration (*Chl*), the concentration of suspended particulate matter (SPM) or the inherent optical properties (IOPs), can be estimated from ρ_w or R_{rs} using bio-optical algorithms [8,9].

Table 1. List of symbols and their descriptions.

Symbol	Description	Units
L_t	radiance at top of atmosphere	W m^{-2} sr^{-1} nm^{-1}
L_w	water-leaving radiance	W m^{-2} sr^{-1} nm^{-1}
R_{rs}	water remote-sensing reflectance	sr^{-1}
r_{rs}	ratio of the upwelling radiance to the downwelling irradiance evaluated just below the surface	sr^{-1}
ρ_t	reflectance at top of atmosphere	—
ρ_{path}	atmospheric path reflectance	—
ρ_r	reflectance from Rayleigh scattering in the absence of aerosol	—
ρ_{aer}	reflectance from aerosol scattering in the absence of gases	—
ρ_{ra}	interaction term between Rayleigh and aerosol scattering	—
ρ_g	sun glint reflectance	—
ρ'_g	estimated sun glint reflectance	—
$\Delta\rho_g$	residual sun glint reflectance	—
ρ_w	water-leaving reflectance	—
ρ_A	aerosol reflectance ($\rho_A = \rho_{aer} + \rho_{ra}$)	—
t_v	total transmittance from water to sensor	—
t_s	total transmittance from solar to water	—
t_{oz}	transmittance of the ozone	—
T	direct transmittance	—
c_0, c_1, c_2	fitting parameters in the polynomial atmospheric model	—
m	wavelength angstrom for aerosol scattering spectrum	—
Chl	chlorophyll concentration	mg/m^3
b_{bNC}	backscattering parameter in a bio-optical ocean reflectance model	m^{-1}
a	total absorption coefficient, $a_w + a_{ph} + a_{dg}$	m^{-1}
a_{dg}	absorption coefficient of the sum of detritus and gelbstoff	m^{-1}
$a_{w,ph}$	absorption coefficient of pure seawater and phytoplankton pigments, respectively	m^{-1}
b_b	total backscattering coefficient, $b_{bw} + b_{bp}$	m^{-1}
$b_{bw,bp}$	backscattering coefficient of pure seawater and suspended particles, respectively	m^{-1}
S	spectral slope parameter of a_{dg}	nm^{-1}
Y	wavelength angstrom of particle backscattering spectrum	—

For the signal detected at TOA, the reflectance ρ_t in general can be written as [10]:

$$\rho_t(\lambda) = t_g(\lambda)[\rho_{path}(\lambda) + t_s(\lambda)t_v(\lambda)\pi R_{rs}(\lambda)] \quad (2)$$

Optics EXPRESS

Here, t_g is the transmittance of the gases (including oxygen, water vapor, ozone, etc.); t_s and t_v represent the atmospheric transmittance from solar to water and water to sensor, respectively. Generally the water-leaving contribution (πR_{rs}) at TOA is much smaller than the atmospheric path reflectance (ρ_{path}), which indeed requires highly accurate AC algorithms to derive reliable R_{rs} for inversions of in-water properties [11].

In the past decades, the development of AC algorithms has achieved great progress [11]. For major satellite ocean color missions such as SeaWiFS and MODIS, the commonly implemented algorithm followed the scheme presented in Gordon and Wang [12] and Wang [13]. In general, "black pixel" (BP), i.e. R_{rs} is negligible, is assumed in near-infrared (NIR) wavelengths (for oligotrophic waters [12]) or in the short-wave infrared (SWIR) wavelengths (for waters with high SPM concentrations [14,15]). Based on this assumption, ρ_t at these wavelengths consist of only atmosphere and surface signals. After removing the Rayleigh-scattering component and surface reflectance, the spectral variation of the remainder is used to search for the two most applicable aerosol models through a pre-defined aerosol look-up table (LUT) generated by radiative transfer simulations (e.g., [16]). Then the selected aerosol models are employed to calculate the aerosol's contribution to ρ_t in the visible spectrum. The main challenge with this algorithm is accounting for the effects of absorbing aerosols [17,18]. When strongly absorbing aerosols, such as soot or dust aerosols, are present in the scene, the BP approach fails because it is difficult to obtain detailed information of strongly absorbing aerosol (its single scattering albedo $\omega_0(\lambda)$ and aerosol optical thickness $\tau_a(\lambda)$) based on measurements in the NIR or SWIR spectral region [17,18]. Moreover, as shown by Gordon [19], the altitude of absorbing aerosols is also a factor affecting the contribution of atmosphere to ρ_t. Therefore, the classical assumption that aerosol's contribution is independent of its altitude no longer holds when there are absorbing aerosols.

Alternative approaches designed to improve AC involving absorbing aerosols have also been proposed, including methods of spectral optimization to determine the aerosol reflectance ρ_A ($\rho_A = \rho_{aer}+\rho_{ra}$) and ρ_w simultaneously. One example was developed by Gordon et al. [19], which adopted more realistic aerosol models specifically to better simulate the spectral variation of the absorbing aerosol contribution to ρ_t, while also took into account the altitude of absorbing aerosols in the atmosphere. In order to find the best ten sets of aerosols, this approach needs to establish LUTs of different aerosol models in advance, therefore it is computationally intensive. Another scheme was proposed by Chomko and Gordon [20], also based on the spectral optimization algorithm, which did not establish LUTs of strongly absorbing aerosol models in advance, but instead applied a revised Junge power-law size distribution of aerosol particles to simulate the aerosol's optical properties ($\omega_0(\lambda)$, $\tau_a(\lambda)$ and the phase function). It is found that such an approach can be applied to aerosols where its absorption index has no dependence on wavelength, e.g., black carbon. However, with colored absorbing aerosols being in present, e.g., dust, the aerosol properties were not well retrieved, as its absorption is a function of wavelength [21]. The above two approaches both employed a bio-optical ocean reflectance model together with the use of the radiative transfer (RT) method to simultaneously estimate water and aerosol optical properties through non-linear optimization of the measured ρ_t.

Recently, Steinmetz et al. [22] proposed a POLYnomial based algorithm to process MERIS measurements (POLYMER), which shows significant improvement in recovering pixels under sun glint. Zhang et al. [23] applied the POLYMER scheme to MODIS measurements for a wide range of water properties, also found improved ability to deal with sun glint and increased data coverage. Further, POLYMER has been applied to Sentinel-2 MSI and Sentinel-3 OCLI data over optical complex waters, and selected as an alternative algorithm with good performance for these measurements [24–26]. Different from the traditional AC schemes that uses LUTs for aerosol contributions in ρ_t, POLYMER assumes that the atmospheric contributions can simply

Optics EXPRESS

be described using a polynomial function of wavelength λ:

$$\rho_{ta}(\lambda) = c_0 + c_1\lambda^m + c_2\lambda^{-4} \tag{3}$$

where ρ_{ta} is the atmospheric reflectance after correction of gaseous absorption, Rayleigh contribution, and initial sun glint effect. c_{0-2} are the fitting parameters with varying units; term $c_2\lambda^{-4}$ represents contributions from Rayleigh-aerosol inter-scattering; and the parameter m represents wavelength angstrom for aerosol scattering spectrum, with a fixed value of -1 used in POLYMER. Then the spectrum of water reflectance can be derived through spectral matching method after combining Eq. (3) with a bio-optical ocean reflectance model [27]. A unique feature of POLYMER is that it does not need a LUT for aerosol contributions. However, as pointed out in Steinmetz et al. [22], it is not clear if POLYMER will perform similarly well if strongly absorbing aerosols exit.

The ocean color community also explored other approaches to deal with satellite R_{rs} in the presence of strongly absorbing aerosols. For instance, Oo et al. [28] placed constraints onto $R_{rs}(410)$ within their AC procedures and reported improved satellite estimations. Wang and Jiang [29] tested an algorithm to force the negative VIIRS $R_{rs}(410)$ values to zero so that the aerosol contributions can be estimated more accurately, leading to ultimately improved R_{rs} products. Furthermore, based on R_{rs} spectral shape, Wei et al. [30] proposed a blue-band estimation algorithm to improve the low-quality satellite R_{rs} in the blue bands for coastal and inland waters.

For all the above schemes, whether it is the LUTs-based scheme or the spectral optimization-based scheme, one common feature is that they all operate on measurements from one sun-sensor geometry for the derivations and treat multiple measurements of the same pixel (e.g., the Geostationary Ocean Color Imager (GOCI) and Himawari-8) independent to each other. One alternative way to improve the performance of atmospheric correction is to maximize the use of information measured from multiangle and polarimetric observations [31–33], such as those from the POLarization and Directionality of the Earth's Reflectance (POLDER), the Research Scanning Polarimeter (RSP) and the Airborne Multiangle SpectroPolarimetric Imager (AirMSPI). For instance, AirMSPI can obtain measurements for a given area from nine viewing angles nearly simultaneously. Xu et al. [31] thus developed a joint retrieval algorithm including a multi-angle smoothing constraint for the AirMSPI dataset using optimization approach. For polar orbiting passive satellite sensors (e.g., MODIS and VIIRS), although no such multi-angle polarization measurements of the same pixel, there could be two or more satellite images for a given area on the same day, with a time gap between the two consecutive overpasses quite short (usually less than 2 hours). For instance, the overlapping areas for VIIRS can be over 50% for latitudes ~26° and increases towards polar regions. We may thus assume the optical properties of marine water during this short period do not vary between the two consecutive satellite measurements, and then use this constraint to achieve better atmospheric correction by combining the two sun-sensor geometries, whereas the atmospheric path reflectance is highly sensitive to viewing geometries. A conceptual diagram of this two-angle atmospheric correction algorithm (TAACA) is shown in Fig. 1, where the atmospheric contributions are different for the two same-day observations, but water contributions remain the same. Note that the water reflectance is less angular dependent for the remote sensing domain [34], and the resulted R_{rs} from satellite can be considered as an "average" ocean reflectance of that short period.

Here we lay out the concept, detailed components, and extensive evaluations of the TAACA scheme that combines two consecutive satellite images in the data processing. The paper is organized such that a brief review of POLYMER is provided first, followed by a detailed description of TAACA. We further show results of applying TAACA to both synthetic and VIIRS measurements, along with discussions of the advantage for improving the quality of retrieved R_{rs} spectrum by TAACA for coastal waters where there are multiple satellite measurements in a day.

Optics EXPRESS

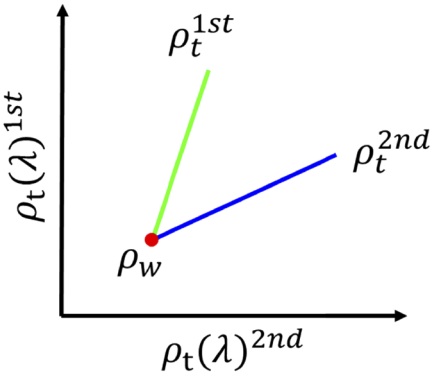

Fig. 1. Conceptual diagram showing the relationship between top-of-atmosphere reflectance (ρ_t) of the same location measured from two different sun-sensor geometries within a short time interval. ρ_w represents the contribution from water, which is assumed to be constant for the two observation geometries; ${\rho_t}^{1st}$ and ${\rho_t}^{2nd}$ represent ρ_t from the two sun-sensor geometries.

2. AC algorithm based on two-angle observations

2.1. Brief overview of POLYMER

Here a brief summary of the POLYMER atmospheric correction scheme [22] is presented for understanding the basis of TAACA. In Eq. (2), ρ_{path} involves various processes associated with radiative transfer in the atmosphere, where ρ_t can be decomposed as [12]:

$$\rho_t(\lambda) = t_{oz}(\lambda)[\rho_r(\lambda) + \rho_{aer}(\lambda) + \rho_{ra}(\lambda) + T(\lambda)\rho_g + t_s(\lambda)t_v(\lambda)\pi R_{rs}(\lambda)] \tag{4}$$

t_{oz} is the transmittance of the ozone layer, ρ_r is the Rayleigh reflectance due to multiple scattering without aerosol, ρ_{aer} is the aerosol reflectance due to multiple scattering without air molecule, ρ_{ra} accounts for the various coupling term between air molecular and aerosol scattering, ρ_g is due to sun glint, T is the direct transmittance, and R_{rs} is the remote-sensing reflectance determined by optical properties of water. Note that the terms for gas (e.g., oxygen and water vapor) effects are omitted as they are either avoided in band design or can be easily calculated using gas information [12,13].

The goal of atmospheric correction is to obtain precise R_{rs} from Eq. (4), which requires accurate estimation of the other components. Specifically, t_{oz} is calculated as following:

$$t_{oz}(\lambda) = \exp[-\tau_{oz}(\lambda)(1/\cos(\theta_o) + 1/\cos(\theta_v))] \tag{5}$$

where τ_{oz} is ozone optical thickness determined from the total ozone concentration U_{oz} (Dobson Unit) obtained from ECMWF data (European Centre for Medium-Range Weather Forecasts). θ_o is the solar zenith angle and θ_v is the satellite viewing zenith angle.

ρ_r is searched from a LUT calculated by the Successive Order of Scattering radiative transfer code (SOS) [35]. $T\rho_g$ is calculated combining the Cox and Munk [36] model with wind speed from the ECMWF data, represented as ρ'_g, with the residual glint represented as $\Delta\rho_g$. Also, the terms $t_s t_v$ are saved in LUTs based the calculation using the SOS code in advance.

After knowing t_{oz}, ρ_r and ρ'_g in ρ_t, Eq. (4) can be rewritten as:

$$\frac{\rho_t(\lambda)}{t_{oz}(\lambda)} - \rho_r(\lambda) - \rho'_g(\lambda) = \Delta\rho_g + \rho_{aer}(\lambda) + \rho_{ra}(\lambda) + t_s(\lambda)t_v(\lambda)\pi R_{rs}(\lambda) \tag{6}$$

Optics EXPRESS

If we replace the left side of Eq. (6) as ρ' and the first three terms of the right side as ρ_{ta}. Then Eq. (6) can be rewritten as:

$$\rho'(\lambda) = \rho_{ta}(\lambda) + t_s(\lambda)t_v(\lambda)\pi R_{rs}(\lambda) \tag{7}$$

The basic principle of the POLYMER algorithm is to model ρ_{ta} using a polynomial function of wavelength as Eq. (3). c_0 represents the spectrally flat components including the residual sun glint and the scattering contributions due to thin clouds and coarse mode aerosols. $c_1\lambda^m$ with the value of m fixed as -1 describes the spectral dependence of the aerosol signal, and $c_2\lambda^{-4}$ characterizes the residual glint along with the couplings between the aerosol and Rayleigh scattering. Substituting Eq. (3) into Eq. (7) leads to:

$$\rho'(\lambda) = c_0 + c_1\lambda^{-1} + c_2\lambda^{-4} + t_s(\lambda)t_v(\lambda)\pi R_{rs}(\lambda) \tag{8}$$

where R_{rs} is further modelled using a bio-optical ocean reflectance model with two parameters: *Chl* and a backscattering coefficient b_{bNC} [37]. Therefore, Eq. (8) can be further written as:

$$\rho'(\lambda) = c_0 + c_1\lambda^{-1} + c_2\lambda^{-4} + t_s(\lambda)t_v(\lambda)\pi R_{rs}(Chl, b_{bNC}, \lambda) \tag{9}$$

Using a simplex method [38], the five parameters (c_0, c_1, c_2, and *Chl*, b_{bNC}) can be derived with the best spectral fit of ρ' through a spectral matching optimization. From the retrieved parameters (c_0, c_1, c_2), R_{rs} is then calculated as:

$$R_{rs}(\lambda) = \frac{\rho'(\lambda) - (c_0 + c_1\lambda^{-1} + c_2\lambda^{-4})}{t_s(\lambda)t_v(\lambda)\pi} \tag{10}$$

2.2. AC based on two sun-sensor viewing geometry observations

2.2.1. Modification of the atmospheric model

In the standard POLYMER system, the parameter m in Eq. (3) is set as -1, which implies a spectral variation from non-absorbing aerosols. In the condition of strongly absorbing aerosols, the value of -1 for parameter m may not correctly account for the aerosol effects. In our new development, m is considered as a variable in the AC process. Consequently, the atmospheric parameters in the spectral optimization are m and c_{0-2}. Meanwhile, we replaced λ in Eq. (3) with the ratio of 400 nm to λ (in nm), thus Eq. (3) is rewritten as:

$$\rho_{ta}(\lambda) = c_0 + c_1(400/\lambda)^m + c_2(400/\lambda)^4 \tag{11}$$

The essence of Eq. (11) is the same as Eq. (3), but the units of c_{0-2} are reflectance, rather vague or varying as in Eq. (3).

2.2.2. Modification of the water remote-sensing reflectance model

The ocean reflectance in POLYMER is represented by two parameters: *Chl*, and a backscattering coefficient b_{bNC} so that at each wavelength $R_{rs} = R_{rs}(Chl, b_{bNC})$. However, this model is not applicable in coastal waters where at least the detritus and gelbstoff (dg) will not co-vary with *Chl*, and these components have significant impact on R_{rs} in the blue bands. Here we adopt an IOP-based remote-sensing reflectance model [39], with the various components and flowchart shown in Fig. 2. To briefly summarize, the total absorption coefficient (a) is a sum of the contributions of pure seawater (a_w), phytoplankton pigments (a_{ph}), and detritus-gelbstoff (a_{dg}). The total backscattering coefficient (b_b) is a sum of that of pure seawater (b_{bw}) and suspended particles (b_{bp}). Values of a_w and b_{bw} are kept as constant, and are taken from Lee et al. [40] and Pope and Fry [41], and Morel [42], respectively. a_{ph}, a_{dg}, and b_{bp} vary with aquatic environment, which are modelled as a function of wavelength (see details in Fig. 2). For spectral slope of a_{dg}

Optics EXPRESS

(S), a representative average of 0.016 nm^{-1} is used. Parameter Y represents the spectral variation of b_{bp}, which is required to be known in order to obtain a b_{bp} spectrum. The values of Y can vary over a range of ~0-2.0 [8], which can influence the retrieval of R_{rs}. The determination of Y in TAACA will be described in detail in section 2.2.3.

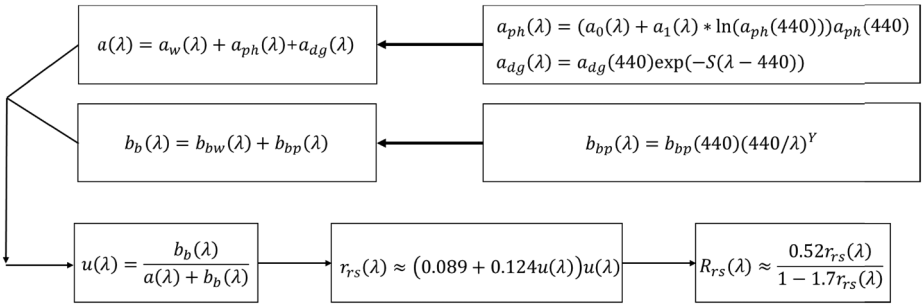

Fig. 2. Components and flowchart of the inherent optical properties used to model remote-sensing reflectance (R_{rs}), in order to estimate top-of-atmosphere reflectance.

Given the various models for a_{ph}, a_{dg}, and b_{bp} spectra, the IOP-based remote-sensing reflectance can be written as

$$R_{rs}^{\mathrm{mod}}(\lambda) = f[a_{ph}(\lambda), a_{dg}(\lambda), b_{bp}(\lambda)] \tag{12}$$

For rigorous evaluation of satellite R_{rs} products, it is recommended to consider the BRDF effect of water-leaving reflectance (e.g., [43]). However, since the R_{rs} in the remote-sensing domain varies less than ~15% for a wide range of sun-sensor geometries [34], for this prove-of-concept study we omit this slight angular variation when modelling $R_{rs}(\lambda)$ for the two sun-sensor angular geometries. In addition, it is because that the influence of this factor is likely much smaller compared with other factors in the AC process, although theoretically such variations can be incorporated in the processing system [44].

2.2.3. Retrieval of water and atmospheric properties from two-angle observations

Among the modified atmospheric and oceanic R_{rs} models, there are seven free variables (m, c_0, c_1, c_2, $a_{ph}(440)$, $a_{dg}(440)$, and $b_{bp}(440)$) for each measured ρ_t spectra, which is an underdetermined system and is difficult to solve for band settings like VIIRS. While atmospheric contributions are highly dependent on solar and viewing geometry, and assuming that water's optical properties do not vary within the short time interval during a day, we thus propose to employ ρ_t from two sun-sensor geometries measured of two consecutive images to solve oceanic and atmospheric properties simultaneously (see the conceptual diagram of Fig. 1). Therefore, the objective of TAACA scheme is to find a set of optimized values for both atmospheric and oceanic parameters described above to achieve the best spectral fit of $\rho_t(\lambda)$ for two different sun-sensor angular geometries on the same day. Because $\rho_w(\lambda)$ is kept the same for the two $\rho_t(\lambda)$ measurements, it works as a constraint of the lower boundary of the coupled atmosphere-ocean system (see Fig. 1), TAACA thus offers an innovative approach to handle atmospheric correction, especially when there are absorbing aerosols. On the other hand, because water properties are kept the same when processing the two consecutive measurements, the final retrieved R_{rs} is a representation of the "averaged" water properties of the two.

We omit the effect of high sun glint by focusing on measurements away from the sun glint geometry. In the standard POLYMER system, Steinmetz et al. [22] utilized a polynomial function as Eq. (3) to represent the atmospheric reflectance after Rayleigh correction. However, when strongly absorbing aerosols are present, due to altitude dependence, the commonly developed LUTs for Rayleigh contribution are no longer applicable. Therefore, here we use the similar

Optics EXPRESS

functionality as Eq. (11) for atmospheric reflectance, but with Rayleigh contribution included in the term $c_2(400/\lambda)^4$, which also includes the Rayleigh-aerosol coupled contributions. The TOA reflectance spectrum of a pixel for the first observation (superscript "*i*") is thus modelled as:

$$\hat{\rho}_t^i(\lambda) = t_{oz}^i(\lambda)[c_0^i + c_1^i(400/\lambda)^{m^i} + c_2^i(400/\lambda)^4 + t_s^i(\lambda)t_v^i(\lambda)\pi R_{rs}^{\mathrm{mod}}(\lambda, a_{ph}(440), a_{dg}(440), b_{bp}(440))] \tag{13}$$

and the TOA reflectance spectrum of the same pixel for the second observation (superscript "*j*") is then as:

$$\hat{\rho}_t^j(\lambda) = t_{oz}^j(\lambda)[c_0^j + c_1^j(400/\lambda)^{m^j} + c_2^j(400/\lambda)^4 + t_s^j(\lambda)t_v^j(\lambda)\pi R_{rs}^{\mathrm{mod}}(\lambda, a_{ph}(440), a_{dg}(440), b_{bp}(440))] \tag{14}$$

As previously described, the absorption of oxygen and water vapor are also omitted in these expressions. With the above considerations, there are eleven unknown variables for spectral optimization: ${c_0}^i$, ${c_1}^i$, ${c_2}^i$, m^i, ${c_0}^j$, ${c_1}^j$, ${c_2}^j$, m^j, $a_{ph}(440)$, $a_{dg}(440)$ and $b_{bp}(440)$. The variation of the atmospheric reflectance is included in the values of parameters (${c_0}^i$, ${c_1}^i$, ${c_2}^i$, m^i) and (${c_0}^j$, ${c_1}^j$, ${c_2}^j$, m^j). The cost function for the spectral optimization is defined as the *err* function similar to Lee et al. [45]:

$$err = 0.5 \times err1 + 0.5 \times err2 \tag{15a}$$

$$err1 = \frac{\sqrt{\frac{\sum_{410}^{862}(\rho_t^i - \hat{\rho}_t^i)^2}{7} + \frac{\sum_{410}^{862}(\rho_t^j - \hat{\rho}_t^j)^2}{7}}}{(\sum_{410}^{862}\rho_t^i)/7 + (\sum_{410}^{862}\rho_t^j)/7} \tag{15b}$$

$$err2 = \frac{\sqrt{\frac{\sum_{410}^{862}(R_{rs}^{\mathrm{mod},i} - \frac{(\rho'^{,i} - \rho_{ta}^{\mathrm{mod},i})}{\pi t_s^i t_v^i})^2}{7} + \frac{\sum_{410}^{862}(R_{rs}^{\mathrm{mod},j} - \frac{(\rho'^{,j} - \rho_{ta}^{\mathrm{mod},j})}{\pi t_s^j t_v^j})^2}{7}}}{(\sum_{410}^{862}R_{rs}^{\mathrm{mod},i})/7 + (\sum_{410}^{862}R_{rs}^{\mathrm{mod},j})/7} \tag{15c}$$

with *err*1 measuring the minimization of ρ_t of the two measurements, while *err*2 measuring the minimization of R_{rs}. A use of combination between *err*1 and *err*2, rather than *err*1 alone, helps to achieve stable optimization outputs.

We adopt the SOLVER tool in Microsoft Excel to minimize this *err* in Eq. (15a) through non-linear GRG optimization algorithm [46]. The settings of optimization option include the precision of 1×10^{-7} and a convergence of 0.0001. In the optimization process, the fitting parameters are forced to be within a reasonable range in natural environment and are listed in Table 2.

Table 2. Range of parameters for both atmosphere and ocean. Min and Max indicate the lower and upper boundaries of these parameters in TAACA.

Parameter	${c_0}^i$	${c_1}^i$	${c_2}^i$	m^i	${c_0}^j$	${c_1}^j$	${c_2}^j$	m^j	$a_{ph}(440)$	$a_{dg}(440)$	$b_{bp}(440)$
Units	—	—	—	—	—	—	—	—	m^{-1}	m^{-1}	m^{-1}
Min	0	0	0	0	0	0	0	0	0.005	0.002	0.001
Max	—	—	—	4	—	—	—	4	0.5	0.6	0.8

For nonlinear optimization, the initial values could be important for final optimization results when the function is complex. We use three rounds of spectral optimization to minimize the impact of initial values, with details of the iterative process described below.

1) With an assumption of the water reflectance at two NIR bands (745 and 862 nm) and two SWIR bands (1238 and 1601 nm) being negligible, we first calculate the values of ${c_0}^i$, ${c_1}^i$,

Optics EXPRESS

$c_2{}^i$, m^i and $c_0{}^j$, $c_1{}^j$, $c_2{}^j$, m^j (they are collectively termed as *atmos* in the following) obtained by the polynomial fit for these four wavelengths of each observation:

$$\rho'^{,i}(\lambda) \approx c_0^i + c_1^i(400/\lambda)^{m^i} + c_2^i(400/\lambda)^4 \tag{16a}$$

$$\rho'^{,j}(\lambda) \approx c_0^j + c_1^j(400/\lambda)^{m^j} + c_2^j(400/\lambda)^4 \tag{16b}$$

2) We use these *atmos* values and the lower boundary values of the water parameters (see Table 2) as the initial guess of the eleven unknown variables, along with a fixed Y value of 0.8 based on the NOMAD data set [47], to carry out the first round of spectral optimization. This step produces first-round remote-sensing reflectance ($R_{rs,1}$) and new values for atmospheric parameters *atmos*.

3) A new set of initial values for the inherent optical properties IOPs are calculated as follows [39]:

$$a_{ph,1}(440) = 0.072[R_{rs,1}(443)/R_{rs,1}(550)]^{-1.62} \tag{17a}$$

$$a_{dg,1}(440) = a_{ph,1}(440) \tag{17b}$$

$$b_{bp,1}(440) = 30a_w(670)R_{rs,1}(670) \tag{17c}$$

Further, an estimate of Y value for each pixel is obtained using an empirical relationship [48],

$$Y_1 \approx 2[1 - 1.2exp(-0.9\chi)] \tag{18}$$

with $\chi = R_{rs,1}(443)/R_{rs,1}(551)$.

4) Using Y_1 values and the new initial values for IOPs and *atmos*, a second round of optimization is carried out to derive both water and atmospheric properties by TAACA, subsequently new remote-sensing reflectance ($R_{rs,2}$) is retrieved. With these $R_{rs,2}$, a new set of initial values of IOPs and Y are estimated following the approaches of the previous round, and a new round of spectral optimization is carried out, which resulted in another set of R_{rs} ($R_{rs}{}^{TAACA}$) and atmospheric properties. These are considered the final outputs through TAACA, as sensitivity tests show no significant difference with more iterations. A schematic chart of the above process of TAACA is shown in Fig. 3, and the differences between POLYMER and TAACA are summarized in Table 3.

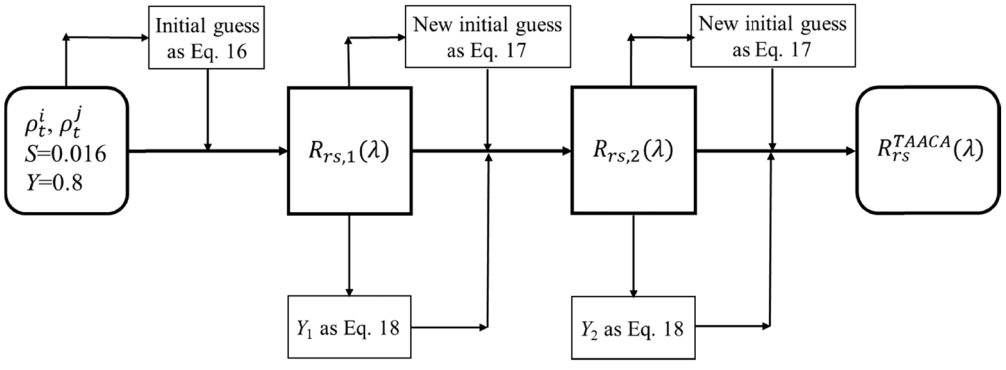

Fig. 3. Flowchart and the iterations of TAACA to obtain $R_{rs}(\lambda)$ from Level 1 top-of-atmosphere reflectance.

Optics EXPRESS

Table 3. Comparison of ocean reflectance model, atmospheric reflectance model and the method of spectral optimization between standard POLYMER and TAACA.

	POLYMER	TAACA
Ocean reflectance model	$R_{rs}(\lambda, Chl, b_{bNC})$ (Morel and Maritorena, 2001) BRDF is not considered	R_{rs} (λ, $a_{ph}(440)$, $a_{dg}(440)$, $b_{bp}(440)$) (Lee et al., 1999) BRDF is not considered
Atmospheric reflectance model	$c_0 + c_1\lambda^{-1} + c_2\lambda^{-4}$ Three unknown variables: c_0, c_1, c_2 With correction of ozone absorption and Rayleigh scattering	$c_0 + c_1(400/\lambda)^m + c_2(400/\lambda)^4$ Four unknown variables: c_0, c_1, c_2, m With correction of ozone absorption
Data used in the processing	Measurement from one sun-sensor geometry	Measurements from two same-day sun-sensor geometries
Method of spectral optimization	Simplex method	"Solver" in Microsoft Excel
Cost function	Mean square error of ρ^*	Similar to Lee et al., [42]

Different from the target of POLYMER for processing MERIS data, here the target is VIIRS measurements, and the spectral bands are adjusted accordingly, where the visible bands (i.e., 410, 443, 486, 551 and 671 nm) and NIR bands (i.e., 745 and 862 nm) are employed in TAACA spectral optimization.

2.3. Metrics to measure algorithm performance

To quantitatively evaluate the performance of TAACA and other AC algorithms, we adopt the following metrics as a quantitative measure, including the root mean square error (RMSE), unbiased root mean square error (uRMSE), and bias (δ). They are calculated as

$$RMSE = \sqrt{\frac{\sum_{i=1}^{N}(Q_{i,1} - Q_{i,2})^2}{N}} \tag{19a}$$

$$uRMSE = \sqrt{\frac{\sum_{i=1}^{N}(2 \times (Q_{i,1} - Q_{i,2})/(Q_{i,1} + Q_{i,2}))^2}{N}} \tag{19b}$$

$$\delta = \frac{\sum_{i=1}^{N}(Q_{i,1} - Q_{i,2})}{N} \tag{19c}$$

where $Q_{i,1}$ and $Q_{i,2}$ refer to the retrieved products and the simulated (or measured) properties, respectively, and N is the number of matching pairs.

We further use the cosine distance to measure the spectral similarity between the retrieved and simulated R_{rs} spectra [e.g. [49]],

$$\cos(\alpha) = \frac{\sum_{i=1}^{N} Rrs_{sim,i} Rrs_{ret,i}}{\sqrt{\sum_{i=1}^{N}(Rrs_{sim,i})^2}\sqrt{\sum_{i=1}^{N}(Rrs_{ret,i})^2}} \tag{20}$$

with α the angle between the simulated (or measured) $R_{rs,sim}$ and the retrieved $R_{rs,ret}$ spectrum. A smaller angle indicates closer matches of the two spectra.

Optics EXPRESS

3. Validation with synthetic data

3.1. Generation of synthetic data

We first verified the feasibility of TAACA with a synthetic dataset, which was generated by a Coupled Ocean Atmosphere Radiative Transfer (COART) model [50] based on the Santa Barbara DISORT Atmospheric Radiative Transfer (SBDART) code [51], with ocean contribution simulated by Hydrolight [52]. The ocean reflectance was simulated with $a_{ph}(440)$, $a_{dg}(440)$, and $b_{bp}(440)$ ranging from 0.02 to 0.2 m^{-1}, 0.02 to 0.2 m^{-1}, and 0.005 to 0.035 m^{-1}, respectively, for which seven values equally spaced. For each combination of IOP parameters, a variety of atmospheric conditions were used:

(1) Variable observation geometries: two relative azimuth angles (30° and 120°), three solar zenith angles (35°, 45°, and 55°), and three sensor viewing zenith angles (40°, 50°, and 60°);

(2) Variable optical thicknesses of aerosol at 865 nm: 0.1, 0.2 and 0.3;

(3) Four aerosol models by combining Shettle and Fenn [16] with Ahmad et al. [53]: O50, O90, U50 and U90;

(4) The altitudes of aerosol layer are at 3 km and 5 km.

The center wavelength of simulated TOA reflectance is set following VIIRS, and the resulted range of R_{rs} is ~0.0001–0.04 sr^{-1} for these wavelengths. Both non-absorbing aerosols (oceanic aerosol models) and strongly absorbing aerosols (urban aerosol models) are considered. Then we randomly select any pair of observing geometries (water properties kept the same, no restriction on atmospheric properties) to represent two consecutive observations of the same pixel. As a result, 3,292 cases were compiled, of which half are non-absorbing and half are strongly absorbing aerosol cases. The simulated TOA reflectance were then processed with TAACA, and the retrieved products (R_{rs} spectra and the inherent optical properties ($a(440)$ and $b_{bp}(440)$)) are compared with those from COART.

3.2. Performance of TAACA with the synthetic dataset

It is found that TAACA performed very well with the synthetic dataset, especially for cases of strongly absorbing aerosols. Scatterplots are shown in Fig. 4 for a visual comparison, with detailed statistical evaluations presented in Table 4. Specifically, for both non-absorbing and strongly absorbing aerosols, the biases of the retrieved R_{rs} are the smallest at 486 and 551 nm, with a linear slope close to 1.0 and $R^2 \approx 1.00$ [Figs. 4(c) and 4(d)]. R_{rs} of these two wavelengths also show small values of RMSE (~2.4 ($\times 10^{-4}$) sr^{-1} and 2.1 ($\times 10^{-4}$) sr^{-1}, see Table 4) and uRMSE (~6.6% and ~4.9%, see Table 4). The slope for $R_{rs}(671)$ is also close to 1.0 [Fig. 4(e)], with R^2 value as ~0.98. The two blue wavelengths, 410 nm and 443 nm, show higher uRMSE (~10-12%) due to the much lower R_{rs} values (many values are around 0.0008 sr^{-1}) in these blue wavelengths, but matching likely the best accuracy of obtaining R_{rs} in field measurements [54]. Further, the α values (mean $\alpha \approx 0$) indicate the R_{rs} spectra from TAACA exhibited very high spectral consistency with the simulated R_{rs} spectra. More importantly, the performance of TAACA show no separation between non-absorbing and strongly absorbing aerosols, indicate a strong potential of TAACA for many coastal waters where absorbing aerosols are quite common.

For comparison, we also applied the standard POLYMER algorithm [22] to process the simulated datasets, with results shown in Fig. 5. For non-absorbing aerosols, R_{rs} at each wavelength is also retrieved very well by POLYMER, with very high R^2 values (~0.99) and low RMSE (~4.6×10^{-4} sr^{-1}) and uRMSE (~7.5%) (Table 5). The results also show that the performance of retrieved $R_{rs}(486)$ and $R_{rs}(551)$ [Figs. 5(c) and 5(d)] is better than that of

Optics EXPRESS

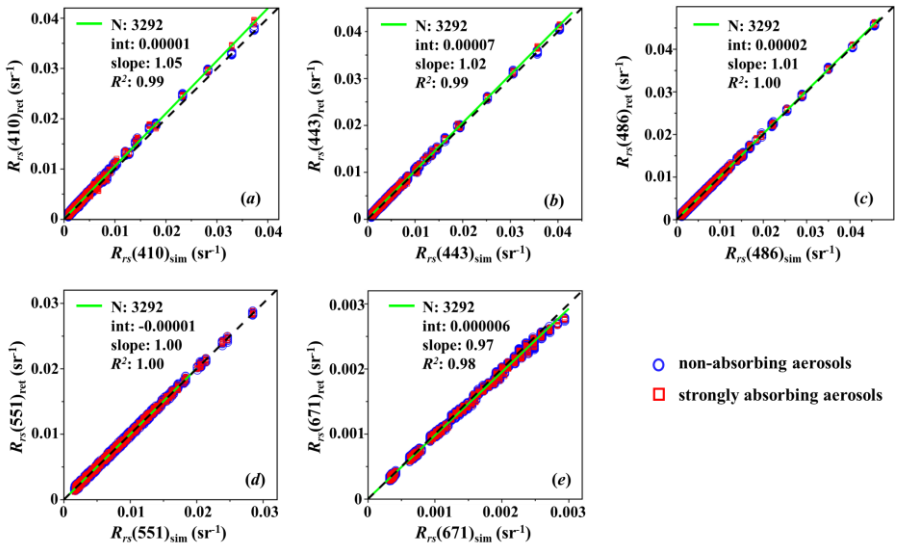

Fig. 4. Scatterplots between the simulated R_{rs} (indicated by subscript "sim") and the TAACA-retrieved R_{rs} (indicated by subscript "ret") for bands 410–671 nm. The black dash-line represents the 1:1 line, and the green line is linear regression of all datasets (both non-absorbing and strongly absorbing aerosols) with the fitting parameters shown in the plots.

Table 4. Statistical results of TAACA retrieved remote-sensing reflectance (R_{rs}) for dataset synthesized by COART. The value within the parentheses for cos(α) refers to its standard deviation.

Band	[a]N		RMSE ($\times10^{-4}$ sr^{-1})		uRMSE (%)		δ ($\times10^{-4}$ sr^{-1})	
	[b]non-absorbing	[c]strongly absorbing	non-absorbing	strongly absorbing	non-absorbing	strongly absorbing	non-absorbing	strongly absorbing
410	1646	1646	4.7	5.5	11.3	12.2	3.2	3.3
443	1646	1646	3.2	3.5	9.3	10.1	1.9	2.0
486	1646	1646	2.3	2.4	6.5	6.6	0.8	0.7
551	1646	1646	2.1	2.1	4.8	4.9	0.1	0.1
671	1646	1646	0.5	0.5	7.3	7.4	-0.3	-0.3
cos(α)	non-absorbing		0.99 (0.0005)					
	strongly absorbing		0.99 (0.0006)					

[a]N is the number of coupled water-atmosphere cases.
[b]non-absorbing refers to the simulated cases with oceanic aerosols.
[c]strongly absorbing refers to the simulated cases with urban aerosols.

R_{rs}(410) and R_{rs}(443) [Figs. 5(a) and 5(b)], which is consistent with the results of TAACA. In contrast, for strongly absorbing aerosols, R_{rs}(410) and R_{rs}(443) retrieved by POLYMER are much lower than known R_{rs}, with uRMSE as ~39.5% and ~22.2%, respectively, for 410 nm and 443 nm (Table 5). These results clearly indicate a necessity to revise the POLYMER scheme for processing measurements associated with strongly absorbing aerosols.

The relationships between the known and retrieved inherent optical properties (a(440) and b_{bp}(440)) by TAACA are presented in Fig. 6. Strong agreements are observed for these inherent optical properties, although the retrieved values are found slightly higher (~8-14%) than known values. This is a result of overestimated Y values [see Eq. (17)] compared to that used in the

Optics EXPRESS

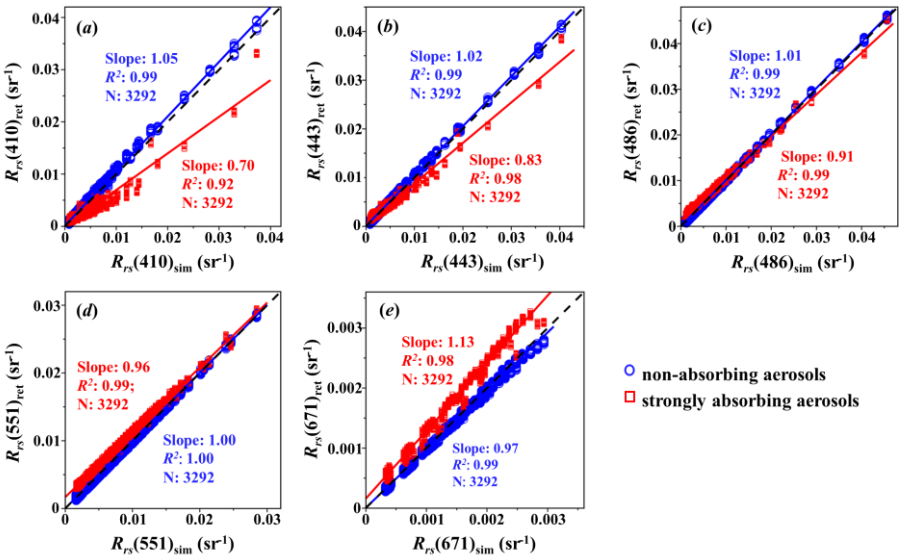

Fig. 5. As Fig. 4, but the synthetic dataset was processed by POLYMER. In these plots, the blue and red lines show linear regression of non-absorbing and strongly absorbing aerosols, respectively, with the fitting parameters shown in the plots.

Table 5. As Table 4, but the COART-synthesized dataset was processed by standard POLYMER.

Band	N[a]		RMSE		uRMSE (%)		δ	
	non-absorbing	strongly absorbing	non-absorbing	strongly absorbing	non-absorbing	strongly absorbing	non-absorbing	strongly absorbing
410	3292	3292	4.6E-4	0.0023	7.5	39.5	3.2E-4	-0.0014
443	3292	3292	2.7E-4	0.0012	4.0	22.2	1.9E-4	-4.0E-4
486	3292	3292	1.1E-4	0.0010	1.3	29.7	7.1E-5	8.1E-4
551	3292	3292	3.9E-5	0.0014	0.7	26.1	1.5E-5	0.0013
671	3292	3292	4.1E-5	3.6E-4	4.0	27.4	-3.1E-5	3.3E-4
cos(α)	non-absorbing		0.99 (0.0002)					
	strongly absorbing		0.98 (0.0058)					

[a]Note here the number is two times that in Table 4 is because that TAACA uses two sun-sensor geometries for each ρ_w (see Fig. 1), while POLYMER uses one sun-sensor geometry for each ρ_w, so the coupled ocean-atmosphere cases for TAACA are half of that for POLYMER, although the number of ρ_w is the same.

simulations (0.8), which then propagated to the estimated IOPs. Again, there are no obvious differences in the performance of non-absorbing versus strongly absorbing aerosols (see Fig. 6), further support the application of TAACA for processing measurements associated with absorbing aerosols.

Optics EXPRESS

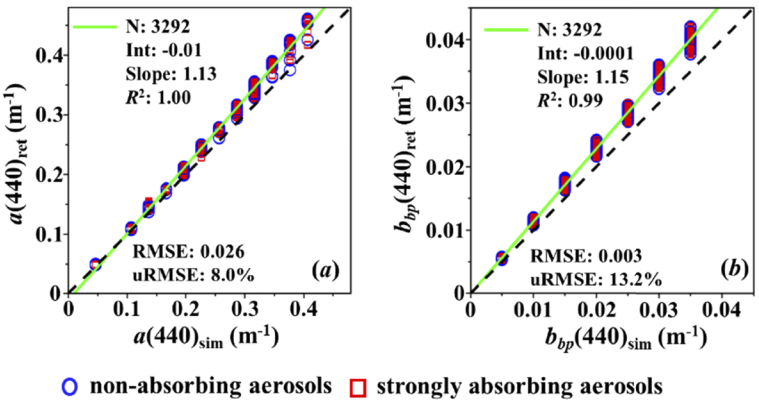

Fig. 6. Scatterplots between synthetic IOPs ($a(440)$ and $b_{bp}(440)$) (indicated by subscript "sim") and the TAACA-retrieved properties (indicated by subscript "ret"). The black dash-line represents the 1:1 line, and the green line is the linear regression of all datasets (both non-absorbing and strongly absorbing aerosols) with the statistical measures shown in the plots.

4. Validation with VIIRS measurements

We further evaluated the performance of TAACA with VIIRS data, where field R_{rs} measurements taken during 2015–2017 over Boston Harbor (BH) and Massachusetts Bay (MB) were used as "ground truth". Massachusetts Bay is a bay on the East Coast of the United States that forms part of the central coastline of the Commonwealth of Massachusetts. As a semi-enclosed bay, water properties and their distribution are largely affected by winds, tides and other factors. Compared with Boston Harbor, the water of Massachusetts Bay is relatively less turbid and dominated by gelbstoff and detritus. Due to its closeness to a populous city, the occurrence of absorbing aerosols is quite common for these regions.

4.1. *In situ measurements*

Field measurements for validation of VIIRS products were carried out in seven days during 2015–2017 in BH-MB, with sampling locations given in Fig. 7. Most of the stations are located in MB, except three stations are located in BH. *In situ* R_{rs} was measured following the skylight-blocked approach (SBA) [55]. Specifically, the water-leaving radiance was directly measured with a hyperspectral radiometer (HyperOCR, Satlantic Inc.), while the downwelling plane irradiance (E_d, $W\ m^{-2}\ nm^{-1}$) was measured by a hyperspectral irradiance radiometer (HyperOCR, Satlantic Inc.). These two radiometers measure signals from ~349.7 to 804.6 nm in 137 spectral channels. All measurement and data processing followed the same protocols as Wei et al. [56]. In 2015, the total absorption coefficient was measured with an AC-S meter (Wetlabs, Inc., Philomath, OR) and the particulate backscattering coefficient was measured with a BB9 sensor (Wetlabs, Inc., Philomath, OR). Due to instrument issues, no AC-S or BB9 measurements were made in 2016 and 2017.

4.2. *VIIRS data*

The VIIRS Level-1 calibrated radiance data were obtained from NOAA's Comprehensive Large Array-data Stewardship System, while Level-2 normalized water-leaving radiance (nL_w) was downloaded from CoastWatch [57], generated by MSL12 (the NOAA Multi-Sensor Level-1 to Level-2 processing system package) [58]. The Level-2 products contain nL_w at bands 410, 443, 486, 551 and 671 nm (nL_w at 745 and 862 nm for MSL12 are not included as operational

Optics EXPRESS

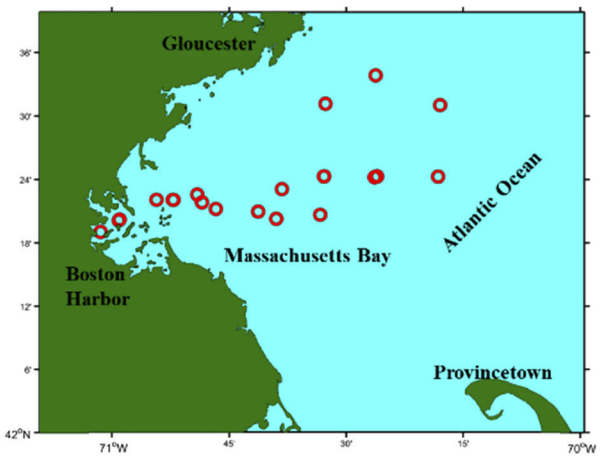

Fig. 7. The locations of the 22 matchup stations (red circles) of seven days for field measurements in Boston Harbor and Massachusetts Bay during 2015–2017. Note that a few stations are at the same locations, so only 18 circles appear in the figure.

products in CoastWatch). To compare *nLw* with *in situ* measurement of R_{rs}, nL_w is converted to R_{rs} following:

$$R_{rs}(\lambda) = nLw(\lambda)/F_0(\lambda) \tag{21}$$

The products generated by MSL12 also contain the Level-2 quality control flags (l2_flags), which were used to exclude questionable R_{rs} spectrum with the following flags: ATMFAIL (atmospheric correction failure), LAND (land pixel), CLDICE (probable cloud or ice contamination), HILT (very high or saturated observed radiance), HIGLINT (strong sun glint contamination), CLDSHDSTL (cloud straylight or shadow contamination) and ATMWARN (atmospheric correction is suspect). In this study, we focused on the sub-scene of BH and MB where *in situ* measurements of R_{rs} are available to validate satellite products.

The time constraint for matchups between *in situ* and VIIRS retrievals is within ±2 h. We eliminated the pairs where the coefficient of variation (CV) within a VIIRS 3 × 3 box centered on the location of *in situ* station is > 0.15 [18], and the number of valid VIIRS R_{rs} retrievals in the box is less than 5 (half of the pixels within this box). Then the mean value of the valid pixels is used as the VIIRS-retrieved value. As a result, twenty-two matchup stations (Fig. 7) from 7 days were obtained for this evaluation.

4.3. Results and discussions

4.3.1. Validation with matchup $R_{rs}(\lambda)$

Figure 8 shows a comparison between *in situ* R_{rs} and VIIRS R_{rs} (bands 410–671 nm) retrieved by TAACA, MSL12 and POLYMER, respectively, for the twenty-two matchup stations from seven days of field measurements. The statistical measures of this comparison for each wavelength are summarized in Table 6. The results of the VIIRS MSL12 R_{rs} products for the first observation ($R_{rs}^{MSL12,1st}$) of the seven days are excluded, as the l2_flags "CLDSHDSTL" and "ATMWARN" are common for these first observations in a day for BH and MB. This is also evidenced by the very low R^2 values (<0.2, not shown) for R_{rs} at 410 nm and 443 nm between the MSL12 products and *in situ* measurements for these first observations in a day. Why the first measurements of VIIRS from the seven days show these flags is an interesting question, but it is beyond the scope of this effort. For the second measurements during a day, as there are no operational products from MSL12 for four stations, MSL12 has just 18 matchup stations. It is necessary to emphasize

Optics EXPRESS

that since TAACA assumes water properties remain the same for the two consecutive VIIRS observations, just one set of R_{rs} spectra are obtained each day from the two VIIRS measurements. Whereas by its architecture in algorithm design, both MSL12 and POLYMER will obtain a set of R_{rs} spectra for each VIIRS observation.

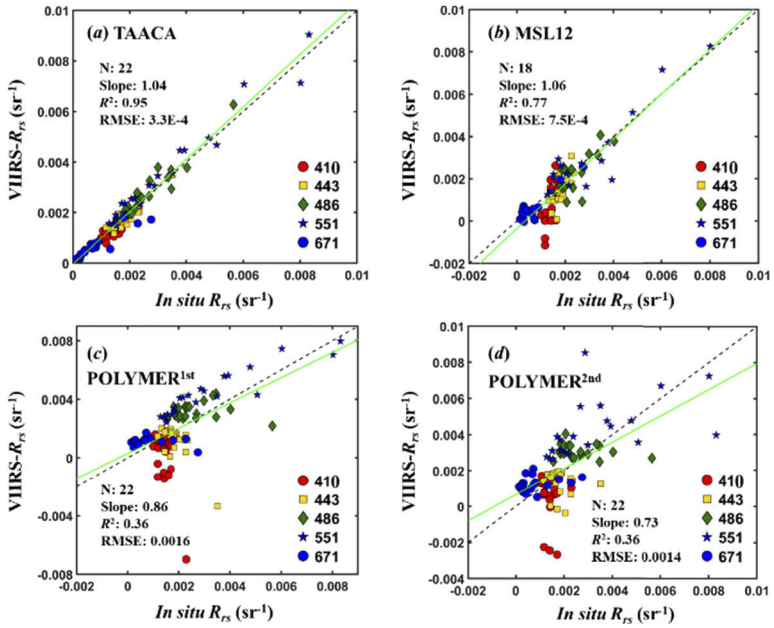

Fig. 8. Scatterplots between VIIRS $R_{rs}(\lambda)$ and *in situ* $R_{rs}(\lambda)$ at bands of 410, 443, 486, 551 and 671 nm for all valid matchup pairs measured in BH-MB during 2015 to 2017. The black dashed line refers to the 1:1 line, and the green line represents linear regression with the statistical measures showing in the plots. (*a*) For results from TAACA; (*b*) For results from MSL12 for the second VIIRS observation; (*c*) For results from POLYMER for the first observation; (*d*) As (*c*), but for results of the second VIIRS observation in a day.

Among the three schemes for atmospheric correction, the R_{rs} retrieved by TAACA (R_{rs}^{TAACA}) matched best with *in situ* R_{rs} ($R_{rs}^{in-situ}$) for the 22 matchup stations, where R^2 is about 0.95 and RMSE is ~3.3×10^{-4} sr^{-1} [Fig. 8(a)]. The parameter of spectral similarity ($\cos(\alpha)$) also shows that TAACA has generated very consistent R_{rs} spectra compared with field measurements (see Table 6). Specifically, the results of each visible wavelength all show strong agreement with *in situ* measurements, where RMSE varies from 2.1 ($\times10^{-4}$) sr^{-1} to 4.9 ($\times10^{-4}$) sr^{-1}, the slope varies from 0.74 to 0.96, and R^2 varies from 0.59 to 0.96 (see Table 6). The retrieved R_{rs}^{TAACA} show the best accuracy at 443 and 486 nm, with RMSE of 2.1 ($\times10^{-4}$) sr^{-1} and 3.4 ($\times10^{-4}$) sr^{-1}, and uRMSE of 12.2% and 11.5%, respectively. At present, $R_{rs}(410)$ indicates higher differences with a slope of 0.74, R^2 of 0.59 and δ of -1.1 ($\times10^{-4}$) sr^{-1}. This is in part because $R_{rs}(410)$ is very low (~0.0015 sr^{-1}) for these dark coastal waters.

In contrast, for these measurements, the performance of the operational R_{rs} products from MSL12 for the second observation ($R_{rs}^{MSL12,2nd}$) in a day exhibits lower accuracy than R_{rs}^{TAACA} at each visible wavelength [Fig. 8(b)], where both RMSE and uRMSE from MSL12 are higher than those from TAACA. Especially, MSL12 significantly underestimated $R_{rs}(410)$, with δ as -7.6 ($\times10^{-4}$) sr^{-1} and R^2 as 0.39 (see Table 6), sometimes $R_{rs}(410)$ even became negative [Fig. 8(b), red dots]. These stations with negative $R_{rs}(410)$ are associated with the l2_flag "ABSAER", indicating the presence and influence of absorbing aerosols, as reported before [59–61].

Optics EXPRESS

Table 6. Statistical measures for all matchup data of R_{rs} derived from TAACA, MSL12 and standard POLYMER algorithms, respectively, for VIIRS measurements in BH-MB.

Band	Scheme	N	RMSE ($\times 10^{-4}$ sr^{-1})	uRMSE (%)	δ ($\times 10^{-4}$ sr^{-1})	Slope	R^2
410	[a]TAACA	22	2.2	17.2	-1.1	0.74	0.59
	MSL12^{2nd}	18	11.0	3890.4	-7.6	3.07	0.39
	POLYMER^{1st}	22	24.0	8384.7	-14.0	-4.11	0.41
	POLYMER^{2nd}	22	16.0	289.9	-8.6	-0.22	0.002
443	TAACA	22	2.1	12.2	-0.6	0.83	0.83
	MSL12^{2nd}	18	6.3	58.9	-3.3	1.67	0.49
	POLYMER^{1st}	22	17.0	1586.4	-6.6	-1.75	0.57
	POLYMER^{2nd}	22	10.0	99.3	-5.2	-0.17	0.02
486	TAACA	22	3.4	11.5	1.7	0.92	0.92
	MSL12^{2nd}	18	6.2	34.1	-1.4	0.95	0.49
	POLYMER^{1st}	22	12.0	41.41	6.1	-0.01	0.0004
	POLYMER^{2nd}	22	12.0	40.8	5.2	-0.10	0.06
551	TAACA	22	4.9	15.3	2.8	0.96	0.96
	MSL12^{2nd}	18	7.7	29.6	0.4	0.99	0.84
	POLYMER^{1st}	22	14.0	47.6	12.0	0.72	0.86
	POLYMER^{2nd}	22	20.0	54.0	10.0	0.41	0.22
671	TAACA	22	3.2	27.3	-1.1	0.87	0.87
	MSL12^{2nd}	18	3.0	94.0	-0.6	0.91	0.80
	POLYMER^{1st}	22	8.7	97.6	3.9	-0.05	0.02
	POLYMER^{2nd}	22	8.3	96.7	4.9	0.17	0.10

cos(α)	TAACA	MSL12^{2nd}	POLYMER^{1st}	POLYMER^{2nd}
	0.99	0.93	0.92	0.93

[a]TAACA stands for results based on processing measurements from two sun-sensor geometries simultaneously. MSL12^{2nd} refers to NOAA's operational products for the second observation. POLYMER^{1st} and POLYMER^{2nd} refer to the products retrieved by POLYMER for the first and second observations, respectively.

For the evaluated VIIRS measurements, POLYMER obtained better performance for R_{rs}(486) and R_{rs}(551), and did not show difference for the two observations in a day [see Figs. 8(c) and 8(d)]. These results are consistent with that reported in previous researches in evaluating the performance of POLYMER for turbid coastal waters [23,24], which showed that the accuracy of retrieved R_{rs} from POLYMER at high blue and green bands are better than that at low blue bands. However, it appears that the standard POLYMER algorithm is also having difficulties for such coastal waters for both observations in a day, although it showed improved performance in dealing with sun glint [22,23]. Compared with MSL12, the performance of these two approaches are comparable at 486 and 551 nm, but the performance of POLYMER is worse than MSL12 at low blue bands, particularly at 410 nm, where the number of negative R_{rs}(410) is much more than that from MSL12 (see Figs. 8(c) and 8(d)]. The reason for the worst performance of the standard POLYMER algorithm for such an environment is that the Rayleigh contributions are also dependent on the altitude of absorbing aerosols [19], thus the commonly developed Rayleigh-reflectance LUTs may not be applicable here as VIIRS cannot provide the altitude information of aerosols. As a result, the atmospheric component in ρ_t after the traditional Rayleigh correction [35] may not be effectively expressed using a polynomial function as Eq. (11). In contrast, TAACA uses a similar polynomial function to simulate the total atmospheric reflectance

Optics EXPRESS

without removing the Rayleigh contribution as an independent step [12], rather to remove the contributions of both Rayleigh and aerosols simultaneously. This approach apparently works better when there are absorbing aerosols, a situation a LUT of Rayleigh reflectance could not be calculated beforehand without knowing the altitude details of such aerosols.

4.3.2. Evaluation of VIIRS R_{rs} image product

The above evaluations with matchup *in situ* R_{rs} show excellent performance of TAACA for waters in BH-MB, where operational MSL12 and standard POLYMER run into difficulties due to the existence of absorbing aerosols. But these are limited to the matchup stations. To gain more insights of TAACA in such a challenging environment, this evaluation is extended to pixels of VIIRS measurements marked by the flag "ABSAER", an indicator of absorbing aerosol in satellite ocean color measurements. As examples, for the second VIIRS observations on September 17th, 2015 and August 1st, 2017 in BH-MB, Figs. 9(a) and 9(e) show the pixels (yellow color) marked by the flag "ABSAER" from MSL12. It is found that most coast pixels indicate the presence of strongly absorbing aerosols, although sometimes the instrument stripping may confuse this flag. After reprojection, the stripping is eliminated in VIIRS Level 2 products as shown in Figs. 9(b)–9(h) [except Fig. 9(e)]. Apparently, due to absorbing aerosols, the R_{rs}(410) values of pixels with the flag "ABSAER" retrieved by MSL12, although generally positive, are very close to 0 [see Figs. 9(b) and 9(f)]. These image products further indicate the impact of strongly absorbing aerosols on the performance of the traditional atmospheric correction algorithm. Also included are results from POLYMER [Figs. 9(c) and 9(g)] for comparison. Although the values of R_{rs}(410) appear more valid in offshore waters, there are many negative values in BH and coastal regions. In contrast, R_{rs}(410) from TAACA [Figs. 9(d) and 9(h)] shows more reasonable values.

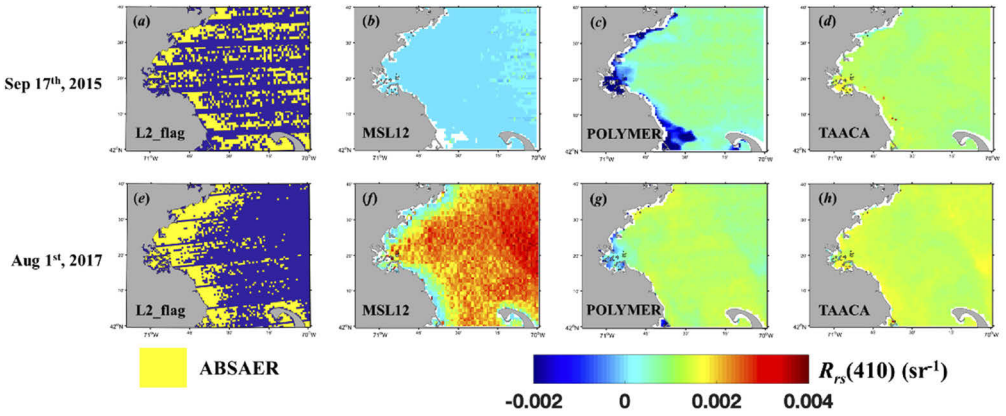

Fig. 9. (*a*) and (*e*) show the spatial distribution of the l2_flag "ABSAER" (yellow color) in BH-MB generated by MSL12 for the second VIIRS observations on September 17th, 2015 (first row) and August 1st, 2017 (second row). (*b*) to (*h*) show VIIRS R_{rs}(410) of images in (*a*) and (*e*) obtained by MSL12, POLYMER, and TAACA, respectively. Note that the stripping effects showing in (*a*) and (*e*) were smoothed out when they are reprojected to Level 2 products.

To further highlight the different performance of these three AC schemes, the statistical distributions of R_{rs}(410) and R_{rs}(443) for the pixels marked by "ABSAER" retrieved by MSL12, POLYMER, and TAACA for the seven days of VIIRS measurements are calculated, respectively, with results shown in Fig. 10. Again, the results from MSL12 correspond to the second VIIRS observation of each day. Also included in Fig. 10 is the histogram of R_{rs}(410) and R_{rs}(443) from

Optics EXPRESS

field measurements. While *in situ* measurements show $R_{rs}(410)$ in a range of 0.001–0.002 sr^{-1} for these waters, $R_{rs}(410)$ values from MSL12 are close to zero, and ~40% from POLYMER having negative $R_{rs}(410)$ [see Fig. 10(a)]. In contrast, $R_{rs}(410)$ values from TAACA show strong agreement with *in situ* measurements. For 443 nm, the distributions of $R_{rs}(443)$ from TAACA, MSL12 and POLYMER [see Fig. 10(b)] show smaller difference compared to that for 410 nm, although $R_{rs}(443)$ from MSL12 appears negatively biased compared to that from TAACA and POLYMER, and that from *in situ* measurements.

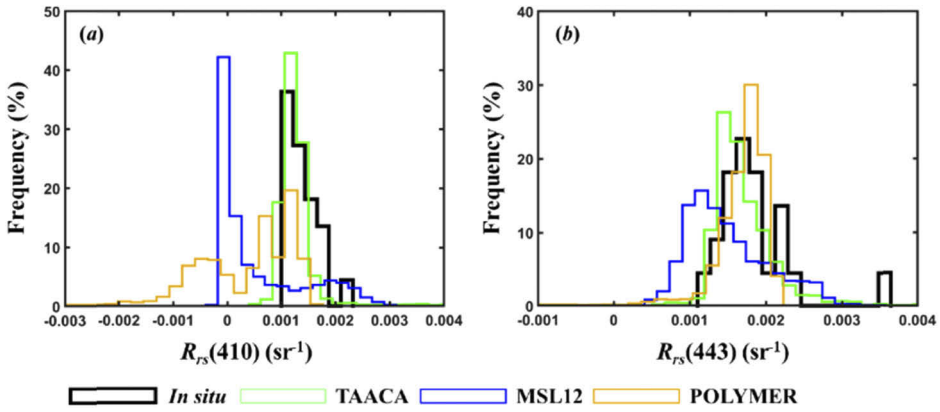

Fig. 10. Statistical distributions of VIIRS $R_{rs}(410)$ (*a*) and $R_{rs}(443)$ (*b*) retrieved by TAACA, MSL12, and POLYMER for the seven days of VIIRS observations over BH-MB in 2015-2017. These are specifically for the pixels marked by the l2_flag "ABSAER". Also included is the distribution of $R_{rs}(410)$ and $R_{rs}(443)$ of this region obtained from *in situ* measurements.

In addition to the evaluation of R_{rs} at a specific wavelength, the quality of the R_{rs} spectra from VIIRS obtained by TAACA, MSL12 and POLYMER, for pixels flagged by "ABSAER" or not, is characterized using the quality assurance (QA) system [49], with results presented in Fig. 11. This is because that such a QA system provides an objective measure of the quality of each R_{rs} spectrum. For the seven days of VIIRS measurements, generally there are less high-quality R_{rs} spectra (QA≥0.8, the highest is 1.0) from MSL12 and POLYMER for pixels flagged by "ABSAER". Specifically, for pixels flagged by "ABSAER", high-quality R_{rs} spectra account for ~40% for results from MSL12 [Fig. 11(a)], while just ~30% for results from POLYMER [Fig. 11(b)]. These results echo the impact of absorbing aerosols on the quality of R_{rs} from MSL12 and POLYMER. In contrast, for pixels with and without the "ABSAER" flag, ~95% of the QA scores for R_{rs} spectra from TAACA are nearly 1.0 [Figs. 11(c) and 11(f)], which are more than double or triple of those from MSL12 or POLYMER. These results further demonstrate the significantly improved R_{rs} products from TAACA for these measurements. Note that when there are absorbing aerosols, schemes like MSL12 and POLYMER require information of the vertical distribution of such aerosols, which could not be available from traditional passive ocean color measurements. Using water properties as a constraint of properties at the lower boundary of the atmosphere-ocean coupled system (see Fig. 1), TAACA is showing strong potentials for improving R_{rs} retrievals when processing satellite ocean color measurements of such kind of environment. It is necessary to point out that both TAACA and POLYMER employed R_{rs} models in the process, but no such R_{rs} model for MSL12, i.e. MSL12 provides an independent retrieval of water signal, therefore higher QA scores could be expected for schemes like TAACA and POLYMER.

Optics EXPRESS

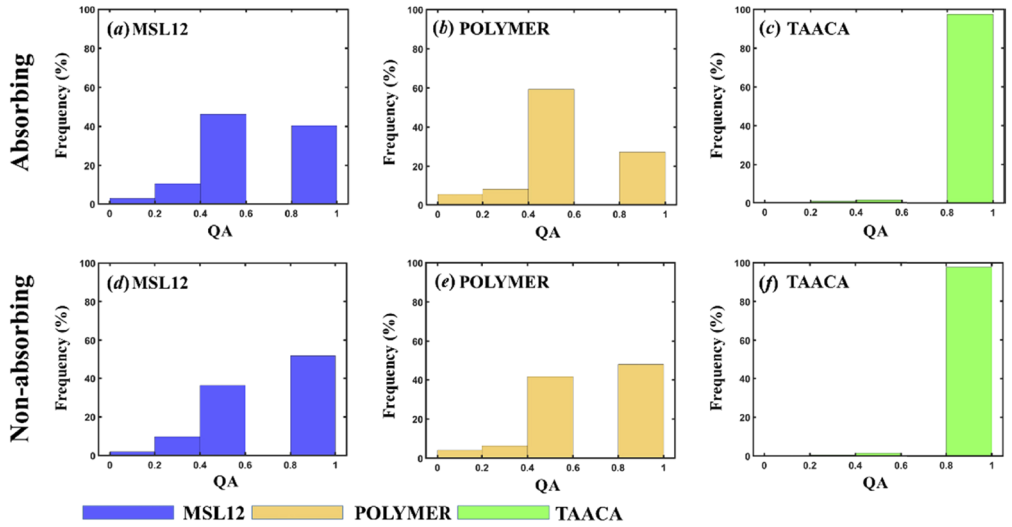

Fig. 11. Distributions of QA scores for the VIIRS-derived R_{rs} from MSL12, POLYMER, and TAACA of the seven days of VIIRS observations in BH-MB during 2015-2017. The first row is for the pixels with the "ABSAER" flag, while the second row is for the pixels without the "ABSAER" flag.

4.3.3. Validation with matchup datasets of IOPs

To further understand the algorithm performance, an extended evaluation of IOPs retrieval from VIIRS ocean color measurements is conducted. Figure 12 presents a comparison between $a(440)$ and $b_{bp}(440)$ estimated from TAACA versus *in situ* measurements made on September 17th and 18th, 2015. Also included are the IOPs derived from ${R_{rs}}^{MSL12,2nd}$, ${R_{rs}}^{POLYMER,1st}$ and ${R_{rs}}^{POLYMER,2nd}$ using the same spectral optimization algorithm, but simply using R_{rs}, rather than ρ_t, as the input. Apparently, both $a(440)$ and $b_{bp}(440)$ retrieved by TAACA show strong agreement with the *in situ* measurements (Fig. 12, green line), where R^2 values are ~0.89 and ~0.95, and uRMSE of ~10.7% and ~20.2%, respectively. For the comparisons of $a(440)$, the performance of POLYMER is better than that of MSL12, but for the results of $b_{bp}(440)$, R_{rs} from MSL12 produced better results. The much higher $a(440)$ from ${R_{rs}}^{MSL12,2nd}$ and ${R_{rs}}^{POLYMER}$ than *in situ* measurements further reflects the lower R_{rs} values in the blue bands from MSL12 and POLYMER (see Fig. 10) due to the appearance of absorbing aerosols as indicated by the "ABSAER" flag.

Due to space limitations and non-essentiality, as examples, the spatial distributions of retrieved $a(440)$ and $b_{bp}(440)$ from ${R_{rs}}^{TAACA}$, ${R_{rs}}^{MSL12,2nd}$, ${R_{rs}}^{POLYMER,1st}$ and ${R_{rs}}^{POLYMER,2nd}$, respectively, for VIIRS measurements on September 17th, 2015 of the study area are presented in Supplement 1. The results show that in general the range of $a(440)$ and $b_{bp}(440)$ from ${R_{rs}}^{MSL12,2nd}$, ${R_{rs}}^{POLYMER,1st}$ and ${R_{rs}}^{POLYMER,2nd}$ are nearly a factor of 2 wider than their ranges of *in situ* measurements, while the ranges of $a(440)$ and $b_{bp}(440)$ from TAACA are consistent with field measurements. These comparisons provide further support of TAACA for processing VIIRS measurements in such a challenging environment.

Optics EXPRESS

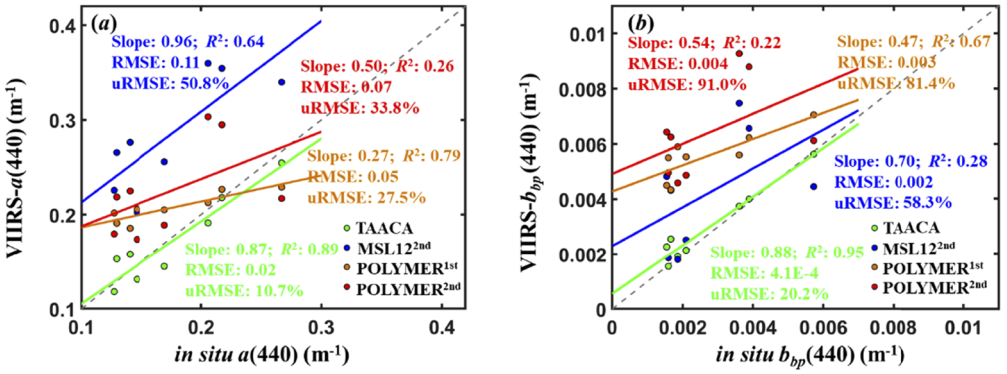

Fig. 12. Comparison between the VIIRS-derived inherent optical properties and *in situ* measurements for VIIRS observations on September 17th and 18th, 2015. (*a*) for $a(440)$ and (*b*) for $b_{bp}(440)$. Results from R_{rs}^{TAACA} (green), $R_{rs}^{MSL12,2nd}$ (blue), $R_{rs}^{POLYMER,1st}$ (yellow), and $R_{rs}^{POLYMER,2nd}$ (red) are presented in different colors.

5. Conclusions

We have developed a novel retrieval scheme – two-angle atmospheric correction algorithm, a.k.a. TAACA – to perform atmospheric correction on satellite ocean color measurements, with a distinctive goal of obtaining improved R_{rs} when there are strongly absorbing aerosols. Unlike conventional atmospheric correction schemes, TAACA takes two (could be extended to more) observations in a day to derive water and atmospheric properties simultaneously, where atmospheric properties are allowed to vary during a day, but water properties are kept the same. In essence, water properties for the two (or more) observation geometries work as a constraint of the lower boundary in the ocean-atmosphere coupled radiative transfer system, thus significantly improved the mathematical solutions of water and atmospheric properties from passive ocean color measurements, especially when there are absorbing aerosols. In particular, because of the use of analytical models for contributions from the atmosphere, TAACA bypasses the need to establish look-up-tables for atmospheric contributions in advance, which is difficult (if not impossible) for strongly absorbing aerosols due to its dependence on the vertical distributions of aerosols. A drawback of TAACA is that water properties are assumed the same for the two observations, which are valid for a relatively short time interval, but will suppress some subtle temporal variations, thus can only be viewed as a temporal average between the two (or more) observations.

Evaluation of TAACA with both synthetic data and VIIRS measurements show strong applicability in coastal waters to obtain robust R_{rs}, especially when there are strongly absorbing aerosols where conventional AC algorithms having difficulties. Compared with both MSL12 and POLYMER, TAACA generated significantly improved R_{rs} in the blue bands for waters of Boston Harbor and Massachusetts Bay from VIIRS measurements. While results of this study show excellent performance of TAACA in handling absorbing aerosols, certainly more evaluations with a wider range of atmosphere and water properties, as well as the impact of the various modeling components, are necessary in order to obtain a complete and comprehensive characterization of TAACA for satellite ocean color remote sensing.

Funding

Ministry of Science and Technology of the People's Republic of China (#2016YFC1400905); National Natural Science Foundation of China (#41830102, #41890803, #41941008); the Joint

Optics EXPRESS

Polar Satellite System (JPSS) funding for the NOAA ocean color calibration and validation (Cal/Val) project; University of Massachusetts Boston.

Acknowledgments

The authors would like to thank CLASS for the distribution of VIIRS Level-1 data products, and CoastWatch for the support of VIIRS Level-2 data products. We also thank three anonymous reviewers for constructive comments and suggestions that greatly helped this manuscript.

Disclosures

The authors declare no conflicts of interest.

See Supplement 1 for supporting content.

References

1. H. R. Gordon, D. K. Clark, J. L. Mueller, and W. A. Hovis, "Phytoplankton pigments from the Nimbus-7 coastal Zone Color Scanner: Comparisons with surface measurements," Science **210**(4465), 63–66 (1980).
2. H. R. Gordon, D. K. Clark, J. W. Brown, O. B. Brown, R. H. Evans, and W. W. Broenkow, "Phytoplankton pigment concentrations in the Middle Atlantic Bight: Comparison of ship determinations and CZCS estimates," Appl. Opt. **22**(1), 20–36 (1983).
3. W. A. Hovis, D. K. Clark, F. Anderson, R. W. Austin, W. H. Wilson, E. T. Baker, D. Ball, H. R. Gordon, J. L. Mueller, S. Z. El-Sayed, B. Strum, R. C. Wrigley, and C. S. Yentsch, "Nimbus-7 Coastal Zone Color Scanner: System descption and initial imagery," Science **210**(4465), 60–63 (1980).
4. S. B. Hooker, W. E. Esaias, G. C. Feldman, W. W. Gregg, and C. R. McClain, "An overview of SeaWiFS and Ocean Color," in *NASA Tech. Memo. 104566, Vol. 1*, S. B. Hooker and E. R. Firestone, eds. (NASA Goddard Space Flight Center, Greenbelt, MD, 1992), p. 24.
5. P. J. Werdell, S. W. Bailey, B. A. Franz, L. W. Harding Jr, G. C. Feldman, and C. R. McClain, "Regional and seasonal variability of chlorophyll-a in Chesapeake Bay as observed by SeaWiFS and MODIS-Aqua," Remote Sens. Environ. **113**(6), 1319–1330 (2009).
6. D. Odermatt, F. Pomati, J. Pitarch, J. Carpenter, M. Kawka, M. Schaepman, and A. Wüest, "MERIS observations of phytoplankton blooms in a stratified eutrophic lake," Remote Sens. Environ. **126**, 232–239 (2012).
7. M. Wang and L. Jiang, "VIIRS-derived ocean color product using the imaging bands," Remote sensing of environment **206**, 275–286 (2018).
8. IOCCG, "Remote Sensing of Ocean Colour in Coastal, and Other Optically-Complex, Waters," in *Reports of the International Ocean-Colour Coordinating Group, No.3*, S. Sathyendranath, ed. (IOCCG, Dartmouth, Canada, 2000).
9. IOCCG, "Remote Sensing of Inherent Optical Properties: Fundamentals, Tests of Algorithms, and Applications," in *Reports of the International Ocean-Colour Coordinating Group, No. 5*, Z.-P. Lee, ed. (IOCCG, Dartmouth, Canada, 2006), p. 126.
10. H. R. Gordon and M. Wang, "Retrieval of water-leaving radiance and aerosol optical thickness over the oceans with SeaWiFS: a preliminary algorithm," Appl. Opt. **33**(3), 443–452 (1994).
11. IOCCG, "Atmospheric Correction for Remotely-Sensed Ocean-Colour Products," in *Reports of the International Ocean-Colour Coordinating Group*, M. Wang, ed. (IOCCG, Dartmouth, Canada, 2010), p. 83.
12. H. R. Gordon and M. Wang, "Retrieval of water-leaving radiance and aerosol optical thickness over oceans with SeaWiFS: A preliminary algorithm," Appl. Opt. **33**(3), 443–452 (1994).
13. M. Wang, "Remote sensing of the ocean contributions from ultraviolet to near-infrared using the shortwave infrared bands: simulations," Appl. Opt. **46**(9), 1535–1547 (2007).
14. M. Wang and W. Shi, "The NIR-SWIR combined atmospheric correction approach for MODIS ocean color data processing," Opt. Express **15**(24), 15722–15733 (2007).
15. B.-C. Gao, M. J. Montes, R.-R. Li, H. M. Dierssen, and C. O. Davis, "An atmospheric correction algorithm for remote sensing of bright coastal waters using MODIS land and ocean channels in the solar spectral region," IEEE Trans. Geosci. Remote Sensing **45**(6), 1835–1843 (2007).
16. E. P. Shettle and R. W. Fenn, "Models for the aerosols of the lower atmosphere and the effects of humidity variations on their optical properties," (Air Force Geophysics Lab Hanscom Afb Ma, 1979).
17. H. R. Gordon, "Atmospheric correction of ocean color imagery in the Earth observing system era," J. Geophys. Res. **102**(D14), 17081–17106 (1997).
18. S. W. Bailey and P. J. Werdell, "A multi-sensor approach for the on-orbit validation of ocean color satellite data products," Remote Sens. Environ. **102**(1-2), 12–23 (2006).

Optics EXPRESS

19. H. R. Gordon, T. Du, and T. Zhang, "Remote sensing of ocean color and aerosol properties: resolving the issue of aerosol absorption," Appl. Opt. **36**(33), 8670–8684 (1997).
20. R. M. Chomko and H. R. Gordon, "Atmospheric correction of ocean color imagery: use of the Junge power-law aerosol size distribution with variable refractive index to handle aerosol absorption," Appl. Opt. **37**(24), 5560–5572 (1998).
21. T. Nakajima, M. Tanaka, M. Yamano, M. Shiobara, K. Arao, and Y. Nakanishi, "Aerosol optical characteristics in the yellow sand events observed in May, 1982 at Nagasaki-Part II Models," J. Meteorol. Soc. Jpn. **67**(2), 279–291 (1989).
22. F. Steinmetz, P.-Y. Deschamps, and D. Ramon, "Atmospheric correction in presence of sun glint: application to MERIS," Opt. Express **19**(10), 9783–9800 (2011).
23. M. Zhang, C. Hu, J. Cannizzaro, D. English, B. B. Barnes, P. Carlson, and L. Yarbro, "Comparison of two atmospheric correction approaches applied to MODIS measurements over North American waters," Remote Sens. Environ. **216**, 442–455 (2018).
24. F. Steinmetz and D. Ramon, "Sentinel-2 MSI and Sentinel-3 OLCI consistent ocean colour products using POLYMER," in *Remote Sensing of the Open and Coastal Ocean and Inland Waters*, (International Society for Optics and Photonics, 2018), 107780E.
25. M. A. Mograne, C. Jamet, H. Loisel, V. Vantrepotte, X. Mériaux, and A. Cauvin, "Evaluation of five atmospheric correction algorithms over French optically-complex waters for the Sentinel-3A OLCI Ocean Color Sensor," Remote Sens. **11**(6), 668 (2019).
26. P. R. Renosh, D. Doxaran, L. D. Keukelaere, and J. I. Gossn, "Evaluation of Atmospheric Correction Algorithms for Sentinel-2-MSI and Sentinel-3-OLCI in Highly Turbid Estuarine Waters," Remote Sens. **12**(8), 1285 (2020).
27. A. Morel and S. Maritorena, "Bio-optical properties of oceanic waters: A reappraisal," J. Geophys. Res.: Oceans **106**(C4), 7163–7180 (2001).
28. M. Oo, M. Vargas, A. Gilerson, B. Gross, F. Moshary, and S. Ahmed, "Improving atmospheric correction for highly productive coastal waters using the short wave infrared retrieval algorithm with water-leaving reflectance constraints at 412 nm," Appl. Opt. **47**(21), 3846–3859 (2008).
29. M. Wang and L. Jiang, "Atmospheric correction using the information from the short blue band," IEEE Trans. Geosci. Remote Sensing **56**(10), 6224–6237 (2018).
30. J. Wei, X. Yu, Z. P. Lee, M. Wang, and L. Jiang, "Improving low-quality satellite remote sensing reflectance at blue bands over coastal and inland waters," Remote Sens. Environ. (to be published) (2020).
31. F. Xu, O. Dubovik, P.-W. Zhai, D. J. Diner, O. V. Kalashnikova, F. C. Seidel, P. Litvinov, A. Bovchaliuk, M. J. Garay, and G. V. Harten, "Joint retrieval of aerosol and water-leaving radiance from multispectral, multiangular and polarimetric measurements over ocean," Atmos. Meas. Tech. **9**(7), 2877–2907 (2016).
32. J. Chowdhary, B. Cairns, M. I. Mishchenko, P. V. Hobbs, G. F. Cota, J. Redemann, K. Rutledge, B. N. Holben, and E. Russell, "Retrieval of aerosol scattering and absorption properties from photopolarimetric observations over the ocean during the CLAMS experiment," J. Atmos. Sci. **62**(4), 1093–1117 (2005).
33. O. P. Hasekamp, P. Litvinov, and A. Butz, "Aerosol properties over the ocean from PARASOL multiangle photopolarimetric measurements," J. Geophys. Res.: Atmos. **116**(D14), D14204 (2011).
34. A. Morel and B. Gentili, "Diffuse reflectance of oceanic waters (2): Bi-directional aspects," Appl. Opt. **32**(33), 6864–6879 (1993).
35. J. Lenoble, M. Herman, J. Deuzé, B. Lafrance, R. Santer, and D. Tanré, "A successive order of scattering code for solving the vector equation of transfer in the earth's atmosphere with aerosols," Journal of Quantitative Spectroscopy and Radiative Transfer **107**(3), 479–507 (2007).
36. C. Cox and W. Munk, "Measurement of the roughness of the sea surface from photographs of the Sun's glitter," J. Opt. Soc. Am. **44**(11), 838–850 (1954).
37. A. Morel and S. Maritorena, "Bio-optical properties of oceanic waters: A reappraisal," J. Geophys. Res. **106**(C4), 7163–7180 (2001).
38. J. A. Nelder and R. J. T. C. J. Mead, "A simplex method for function minimization," Comput. J. **7**(4), 308–313 (1965).
39. Z. Lee, K. L. Carder, C. D. Mobley, R. G. Steward, and J. S. Patch, "Hyperspectral remote sensing for shallow waters: 2. Deriving bottom depths and water properties by optimization," Appl. Opt. **38**(18), 3831–3843 (1999).
40. Z. Lee, J. Wei, K. Voss, M. Lewis, A. Bricaud, and Y. Huot, "Hyperspectral absorption coefficient of "pure" seawater in the range of 350–550 nm inverted from remote sensing reflectance," Appl. Opt. **54**(3), 546–558 (2015).
41. R. Pope and E. Fry, "Absorption spectrum (380 - 700 nm) of pure waters: II. Integrating cavity measurements," Appl. Opt. **36**(33), 8710–8723 (1997).
42. A. Morel, "Optical properties of pure water and pure sea water," in *Optical Aspects of Oceanography*, N. G. Jerlov and E. S. Nielsen, eds. (Academic, New York, 1974), pp. 1–24.
43. A. Morel, D. Antoine, and B. Gentili, "Bidirectional reflectance of oceanic waters: accounting for Raman emission and varying particle scattering phase function," Appl. Opt. **41**(30), 6289–6306 (2002).
44. Z.-P. Lee, K. Du, K. J. Voss, G. Zibordi, B. Lubac, R. Arnone, and A. Weidemann, "An inherent-optical-property-centered approach to correct the angular effects in water-leaving radiance," Appl. Opt. **50**(19), 3155–3167 (2011).
45. Z. P. Lee, K. L. Carder, T. G. Peacock, C. O. Davis, and J. L. Mueller, "Method to derive ocean absorption coefficients from remote-sensing reflectance," Appl. Opt. **35**(3), 453–462 (1996).
46. D. C. Harris, "Nonlinear least-squares curve fitting with Microsoft Excel Solver," J. Chem. Educ. **75**(1), 119 (1998).

Optics EXPRESS

47. S. Maritorena, D. A. Siegel, and A. R. Peterson, "Optimization of a semianalytical ocean color model for global-scale applications," Appl. Opt. **41**(15), 2705–2714 (2002).
48. Z. Lee, B. Lubac, J. Werdell, and R. Arnone, "An update of the quasi-analytical algorithm (QAA_v5)," 1–9 (2009).
49. J. Wei, Z.-P. Lee, and S. Shang, "A system to measure the data quality of spectral remote sensing reflectance of aquatic environments," J. Geophys. Res. Oceans **121**, 8189–8207 (2016).
50. K. P. Du and Z. P. Lee, "Remote-sensing reflectance from above-surface measurements: a revisit based on a coupled ocean-atmosphere model," presented at the *Ocean Optics XXII*, Portland, Maine, U.S.A, 2014.
51. P. Ricchiazzi, S. Yang, C. Gautier, and D. Sowle, "SBDART: A research and teaching software tool for plane-parallel radiative transfer in the Earth's atmosphere," Bull. Am. Meteorol. Soc. **79**(10), 2101–2114 (1998).
52. C. D. Mobley, "Hydrolight 4.0 users guide," (SEQUOIA SCIENTIFIC INC, MERCER ISLAND WA, 1998).
53. Z. Ahmad, B. Franz, C. McClain, E. Kwiatkowska, J. Werdell, E. Shettle, and B. Holben, "New aerosol models for the retrieval of aerosol optical thickness and normalized water-leaving radiances from the SeaWiFS and MODIS sensors over coastal regions and open oceans," Appl. Opt. **49**(29), 5545–5560 (2010).
54. H. Lin, Z. Lee, G. Lin, and X. Yu, "Experimental evaluation of the self-shadow and its correction for on-water measurements of water-leaving radiance," Appl. Opt. **59**(17), 5325–5334 (2020).
55. Z.-P. Lee, N. Pahlevan, Y.-H. Ahn, S. Greb, and D. O'Donnell, "A robust approach to directly measure water-leaving radiance in the field," Appl. Opt. **52**(8), 1693–1701 (2013).
56. J. Wei, Z. Lee, R. Garcia, L. Zoffoli, R. A. Armstrong, Z. Shang, P. Sheldon, and R. F. Chen, "An assessment of Landsat-8 atmospheric correction schemes and remote sensing reflectance products in coral reefs and coastal turbid waters," Remote Sens. Environ. **215**, 18–32 (2018).
57. CoastWatch, "Level-2 warer-leaving radiance," https://coastwatch.noaa.gov/.
58. M. Wang, X. Liu, L. Jiang, S. Son, J. Sun, W. Shi, and V. Lance, "VIIRS ocean color research and applications," *IEEE International Geoscience and Remote Sensing Symposium* 2911–2914 (2015).
59. S. W. Bailey and P. J. Werdell, "A multi-sensor approach for the on-orbit validation of ocean color satellite data products," Remote Sens. Environ. **102**(1-2), 12–23 (2006).
60. S. Hlaing, T. Harmel, A. Gilerson, R. Foster, A. Weidemann, R. Arnone, M. Wang, and S. Ahmed, "Evaluation of the VIIRS ocean color monitoring performance in coastal regions," Remote Sens. Environ. **139**, 398–414 (2013).
61. C. Hu, B. B. Barnes, L. Feng, M. Wang, and L. Jiang, "On the Interplay Between Ocean Color Data Quality and Data Quantity: Impacts of Quality Control Flags," IEEE Geosci. Remote Sensing Lett. **17**(5), 745–749 (2020).